Journal of Solid State Chemistry 182 (2009) 1336–1342

Contents lists available at ScienceDirect

Journal of Solid State Chemistry

journal homepage: www.elsevier.com/locate/jssc

Kinetics of Mn_2O_3 digestion in H_2SO_4 solutions

Daud K. Walanda, Geoffrey A. Lawrance, Scott W. Donne *

Discipline of Chemistry, University of Newcastle, Callaghan, NSW 2308, Australia

ARTICLE INFO

Article history:
Received 12 December 2008
Received in revised form
27 February 2009
Accepted 28 February 2009
Available online 11 March 2009

Keywords:
Manganese dioxide
Hydrothermal synthesis
Disproportionation
X-ray diffraction

ABSTRACT

The kinetics of Mn_2O_3 digestion in various H_2SO_4 solutions (0.5–2.0 M) and at various temperatures (ambient to 80 °C) to form solid γ-MnO_2 and soluble Mn(II) have been examined using X-ray diffraction. Using a modified first-order Avrami expression to describe digestion kinetics, rate constants in the range 0.02–0.98 h^{-1} were found for Mn_2O_3 disappearance, and 0.03–0.42 h^{-1} for γ-MnO_2 formation, with higher H_2SO_4 concentrations and temperatures leading to faster conversion rates. Also, for a particular set of experimental conditions, the rate of γ-MnO_2 formation was always slower than Mn_2O_3 disappearance. This was interpreted in terms of the solubility and stability of the soluble Mn(III) intermediated formed during the digestion. Activation energies for Mn_2O_3 dissolution and γ-MnO_2 formation were also determined.

1. Introduction

Modern society is very dependent on electrical energy. From the home to heavy industry electricity can be found powering devices ranging from an electric arc blast furnace, through the most sophisticated medical apparatus, to the humble toaster. An added benefit of electrical energy is that it can be made portable, and it is in this arena that batteries predominate. Consumers have access to a wide range of battery systems for providing portable power. The choice of the most appropriate battery system depends on the electronic application. However, by far the most common is the alkaline Zn/MnO_2 battery system, which has been available for many decades. There are many reasons for the popularity of this system, but mostly it is because of the properties and performance of the alkaline manganese dioxide cathode. In particular, manganese dioxide with suitably high density and purity, as well as adequate electrochemical activity under a range of discharge conditions, can be produced efficiently and inexpensively on a commercial scale [1].

The phase of manganese dioxide preferred for use in the aqueous alkaline cathode is γ-MnO_2. The basic description of the γ-MnO_2 structure has been attributed to De Wolff [2] who suggested that it consists of a microscopic intergrowth of the ramsdellite and pyrolusite (β-MnO_2) phases of manganese dioxide, as shown in Fig. 1. Since this original description many other researchers have contributed to the understanding of γ-MnO_2 structure. Ruetschi et al. [3] introduced the cation vacancy model to explain some physico-chemical features of γ-MnO_2. This model proposed that some of the Mn^{4+} ions within the structure were absent, with the charge discrepancy compensated by four protons on the surrounding oxide anions to make OH^-. Similarly, some Mn^{4+} ions were found to be reduced to Mn^{3+}, with the charge discrepancy again being compensated by protons on an adjacent oxide anion. The presence of these OH^- groups within the γ-MnO_2 structure constitutes structural water, leading to the following structural description:

$$(Mn^{4+})_{1-x-y} \cdot (Mn^{3+})_y \cdot (\square)_x \cdot (O^{2-})_{2-4x-y} \cdot (OH^-)_{4x+y} \quad (1)$$

where □ represents a cation vacancy, and x and y are the mole fractions of cation vacancies and Mn^{3+} species, respectively. Typical ranges for x and y in a pristine γ-MnO_2 sample are 0.06–0.08 and 0.04–0.12, respectively [4]. Both of these features also decrease the stoichiometry of manganese dioxide to MnO_n, where n ranges from 1.90–1.98. A more recent advance in structural development was made by Chabre and Pannetier [5] who proposed the presence of microtwinning in the (021) and (061) planes within the γ-MnO_2 structure. This model was quite successful in explaining some of the features observed in the X-ray diffraction (XRD) pattern of γ-MnO_2; however, conflicting high resolution TEM data highlights the uncertainty associated with whether microtwinning does actually exist [6,7].

Commercial production of γ-MnO_2 is mostly via electrolysis, leading to the designation electrolytic manganese dioxide (EMD) [8]. Here the EMD is deposited anodically (10–100 A/m^2) onto a titanium substrate from an acidic (0.05–0.5 M H_2SO_4) solution of $MnSO_4$ (0.1–2.0 M) at temperatures over 90 °C. While the ranges for these synthesis variables are quite broad, the specific conditions necessary for making high performance γ-MnO_2 are quite narrow indeed. Following deposition, the EMD is mechanically stripped from the anode then milled to a mean particle size of ~45 μm, washed and neutralized with aqueous NaOH, and then

* Corresponding author. Fax: +61 2 4921 5472.
E-mail address: scott.donne@newcastle.edu.au (S.W Donne).

0022-4596/$ - see front matter © 2009 Elsevier Inc. All rights reserved.
doi:10.1016/j.jssc.2009.02.034

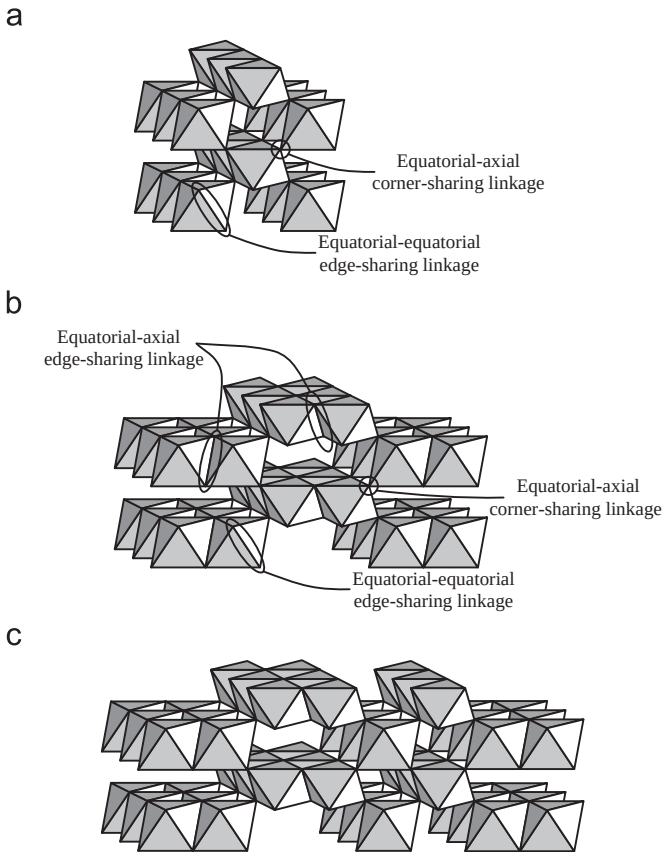

Fig. 1. Schematic structural diagrams of (a) pyrolusite (β-MnO_2); (b) ramsdellite and (c) De Wolff's model for γ-MnO_2 showing the intergrowth between pyrolusite and ramsdellite domains.

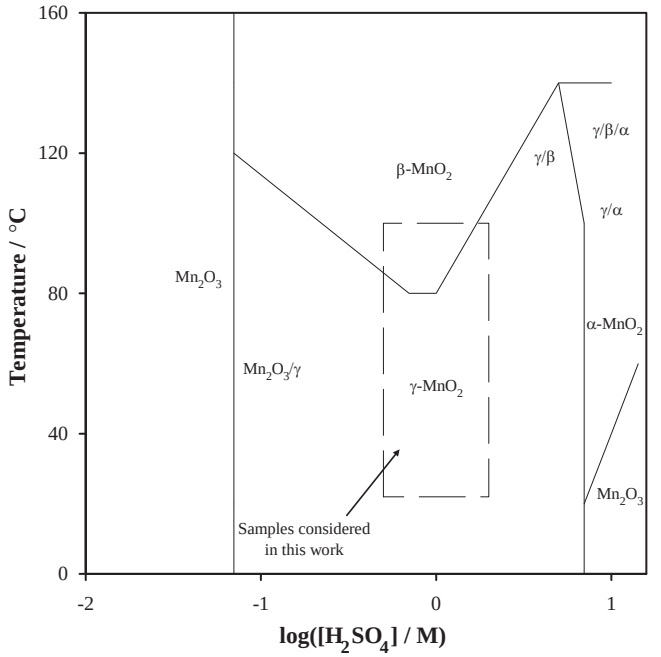

Fig. 2. Manganese dioxide phase diagram resulting from the acid digestion of Mn_2O_3 [12]. Note the dashed box in this figure representing the range of samples examined in this work.

dried before being ready for use. While electrodeposition is the most common approach to making γ-MnO_2 (3×10^5 t per annum), it is by no means the only way. Numerous other methods have been developed [9–11]; however, of most interest to this work is its synthesis via acid digestion of a lower manganese oxide such as Mn_2O_3 or Mn_3O_4 [11]. In our previous work in this area [12] we generated a phase diagram (Fig. 2) detailing the solid state phases that result from the acid (H_2SO_4) digestion of Mn_2O_3. Within the domain of γ-MnO_2 stability, the effects of [H_2SO_4] and temperature were examined and found to impact on the pyrolusite content (P_r), cation vacancy fraction (x) and Mn^{3+} content (y) of the resultant material. Here we report on the effect that these synthesis variables have on the kinetics of γ-MnO_2 phase formation.

2. Experimental

2.1. Starting material and reagents

The Mn_2O_3 starting material was prepared by heating commercially available EMD (Delta EMD Australia Pty Limited) at 550 °C for 24 h, after which time it was phase pure as determined by XRD. Suitable concentrations of H_2SO_4 solutions were prepared by diluting AR grade concentrated H_2SO_4 (Sigma-Aldrich) with ultra-pure Milli-Q water.

2.2. Digestion procedure

The general digestion procedure involved immersing Mn_2O_3 in different concentrations of H_2SO_4 solutions (0.5–2.0 M), at different temperatures (from ambient up to 100 °C), for varying lengths of time (from 3 h up to 4 days). The range of experimental conditions covered is also shown in Fig. 2, emphasizing our focus on the synthesis of γ-MnO_2. The specific synthesis method involved placing separate 10.00 g samples of the Mn_2O_3 starting material into a number of separate 250 mL glass-stoppered Erlenmeyer flasks. The number of flasks chosen was determined by how many data points were to be collected during the kinetic experiment (typically 10). Pre-heated 100 mL aliquots of an appropriate concentration of H_2SO_4 solution were then added to each flask to initiate the digestion process. The identical flasks were then placed into an oven set at the digestion temperature. Each flask was agitated periodically throughout the course of the digestion experiment. After various pre-determined times an individual flask was removed from the oven, filtered and washed thoroughly with ultra-pure Milli-Q water, before being dried in air at 60 °C. The sample was then subjected to an XRD analysis to determine its phase composition.

2.3. XRD Characterization

XRD analysis of each sample was carried out using a Philips 1710 diffractometer equipped with a Cu anode to generate Cu$K\alpha$ radiation ($\lambda = 1.5418$ Å). Each diffraction pattern was collected in the 2θ range 10°–80° using a step size of 0.05° and a count time of 2.5 s per step.

3. Results and discussion

3.1. Digestion thermodynamics

The digestion of Mn_2O_3 in H_2SO_4 solutions is believed to proceed via a dissolution–precipitation mechanism involving disproportionation of a soluble Mn(III) intermediate [12]; i.e.,

$$\text{dissolution}: \quad Mn_2O_3 + 6H^+ \leftrightarrow 2Mn^{3+} + 3H_2O \qquad (2)$$

disproportionation-precipitation :

$$2Mn^{3+} + 2H_2O \leftrightarrow MnO_2 + Mn^{2+} + 4H^+ \quad (3)$$

overall : $$Mn_2O_3 + 2H^+ \leftrightarrow MnO_2 + Mn^{2+} + H_2O \quad (4)$$

The dissolution step in the mechanism (Eq. (2)) was proposed based on the domain of soluble Mn(III) stability in low pH solution in the Eh–pH diagram for the Mn–H_2O system [13]. In short, decreasing the pH (or increasing the acid concentration) leads to the dissolution of more Mn(III) into the electrolyte. The equilibrium constant for this step in the mechanism is given by

$$K_2 = \frac{(a_{Mn^{3+}})^2}{(a_{H^+})^6} = 6.0 \times 10^{-3} \quad (\text{at } 25\ ^\circ C) \quad (5)$$

indicating that this reactants-favoured equilibrium requires a relatively high proton concentration to achieve significant solubilization of Mn(III) [14].

In previous work, Welsh [15] has investigated the disproportionation-precipitation stage of the mechanism as part of a study into the electrodeposition of manganese dioxide. This author determined that the equilibrium constant for Eq. (3) was heavily products-favoured (1.8×10^6 at 15 °C) and increased by an order of magnitude when the temperature was increased (2.0×10^7 at 100 °C). These equilibrium constants were, however, considerably less than that calculated from thermochemical data [14]; i.e.,

$$K_3 = \frac{(a_{Mn^{2+}})(a_{H^+})^4}{(a_{Mn^{3+}})^2} = 3.0 \times 10^9 \quad (\text{at } 25\ ^\circ C) \quad (6)$$

As mentioned by Welsh, the equilibrium constants he determined were based on concentrations rather than activities, which could potentially explain the differences. Combining Eqs. (5) and (6) allows us to determine an overall equilibrium constant for Eq. (4); i.e.,

$$K_4 = K_2 \times K_3 = \frac{(a_{Mn^{2+}})}{(a_{H^+})^2} = 1.7 \times 10^7 \quad (\text{at } 25\ ^\circ C) \quad (7)$$

Of most importance in Eq. (7) is that the overall reaction is very products-favoured. What remains to be determined is the kinetics of this overall process, and what effect acid concentration and temperature have on the rate of reaction.

3.2. Origins of γ-MnO_2 structural variety

Before examining the kinetics of transformation, it is appropriate at this point to comment on the manganese dioxide structural variety within the range of experiments carried out. Within the temperature and H_2SO_4 concentration domain we have chosen for study, previous work has shown that γ-MnO_2 is the manganese dioxide phase produced after seven days of immersion [12]. While γ-MnO_2 is the general crystal structure produced, variability within this classification was apparent in terms of the proportion of pyrolusite present (P_r), the cation vacancy content (x), the Mn^{3+} content (y), as well as the proportion of microtwinning (T_w). Qualitatively, an increase in H_2SO_4 concentration led to a decrease in P_r and y, but an increase in x, whereas an increase in temperature led to an increase in P_r, and a decrease in both x and y. The effects on microtwinning have not been included because the trends in this parameter were not statistically significant.

The approach taken to explain the variations in γ-MnO_2 structure is based on the pyrolusite and ramsdellite structural components, and how the individual octahedra in these domains are interconnected. Examination of the pyrolusite schematic in Fig. 1 shows that there are equatorial–equatorial edge sharing and equatorial–axial corner sharing octahedral linkages. Ramsdellite also has these linkages, as well as equatorial–axial edge sharing linkages, which is what differentiates it from pyrolusite. The manganese dioxide structure formed is determined by the way in which the soluble Mn(III) intermediate condenses from solution. The Mn(III) intermediate is likely to exist in solution as the hexa-aquo complex $[Mn(OH_2)_6]^{3+}$, the condensation of which begins by hydroxylation [16]; i.e.,

$$[Mn(OH_2)_6]^{3+} \leftrightarrow [Mn(OH_2)_5(OH)]^{2+} + H^+ \quad (8)$$

Since Mn(III) is Jahn–Teller distorted, the proton lost is most likely to have come from an equatorial location since there is a higher electron density between the Mn and O (shorter bond), and hence less between O and H. Condensation of the hydroxylated species in Eq. (8) can then occur via (i) olation, which leads to an equatorial–axial corner sharing linkage (common to both pyrolusite and ramsdellite), or (ii) oxolation, to form either an equatorial–equatorial edge sharing linkage or an equatorial-axial linkage [16]. The equatorial–axial linkage formed via oxolation is preferred because it makes use of an axial H_2O molecule as a leaving group. This linkage is also unique to ramsdellite.

The structure of the resultant γ-MnO_2 depends on the relative amount of equatorial–axial corner sharing (olation) and equatorial–axial edge sharing (oxolation). If olation predominates then a high P_r will result. Conversely, if oxolation can occur, then P_r will be low. This may be the result of an exothermic hydrolysis reaction (Eq. (8)), which would shift the equilibrium to the reactants side and hence form fewer hydrolysed Mn(III) molecules. This would result in a lower likelihood of two hydrolyzed Mn(III) molecules colliding and reacting in a concerted fashion. A higher digestion temperature may also provide enough thermal energy to more effectively overcome an activation barrier for olation to occur. Whilst olation must occur to form the γ-MnO_2 structure, a higher temperature may further promote its occurrence.

The H_2SO_4 concentration can influence the digestion process in two ways. Firstly, increasing the H_2SO_4 concentration leads to a more soluble Mn(III) intermediate, thus providing more of the $[Mn(OH_2)_6]^{3+}$ species for subsequent hydrolysis (Eq. (2)). However, increasing the H_2SO_4 concentration would also inhibit the hydrolysis reaction (Eq. (8)), hence limiting condensation by oxolation due to the lack of hydrolyzed Mn(III) species. Clearly a competition exists between these processes, in which fewer $[Mn(OH_2)_5(OH)]^{2+}$ molecules favour olation, and hence a higher P_r value. Since P_r decreases as the H_2SO_4 concentration increases, this suggests that the dissolution reaction (Eq. (2)) to produce more soluble Mn(III) is the dominant reaction, rather than hydrolysis suppression. Therefore, more $[Mn(OH_2)_5(OH)]^{2+}$ molecules are formed increasing the likelihood that equatorial–axial edge sharing linkages will be formed.

3.3. XRD data and analysis

A typical sequence of XRD patterns for the conversion of Mn_2O_3 into MnO_2 is shown in Fig. 3, in this case using 0.7 M H_2SO_4 at ambient temperature. Note the transition from Mn_2O_3 into γ-MnO_2, which is consistent with the phase diagram generated in previous work [12], and shown in Fig. 2. In Fig. 4 we show the sequence of XRD patterns for a set of conditions approaching the phase border between γ- and β-MnO_2 in Fig. 2; i.e., Mn_2O_3 digestion in 1.0 M H_2SO_4 at 80 °C. Here we see that the Mn_2O_3 first transitions to γ-MnO_2 and then to β-MnO_2, suggesting that γ-MnO_2 is formed first as the kinetically stable (metastable) product. In both of these cases, and also in all experiments, the ultimate phase of manganese dioxide that should form is β-MnO_2 because it is the thermodynamically stable phase [14]. Therefore, the domain of γ-MnO_2 stability indicated in Fig. 2 effectively

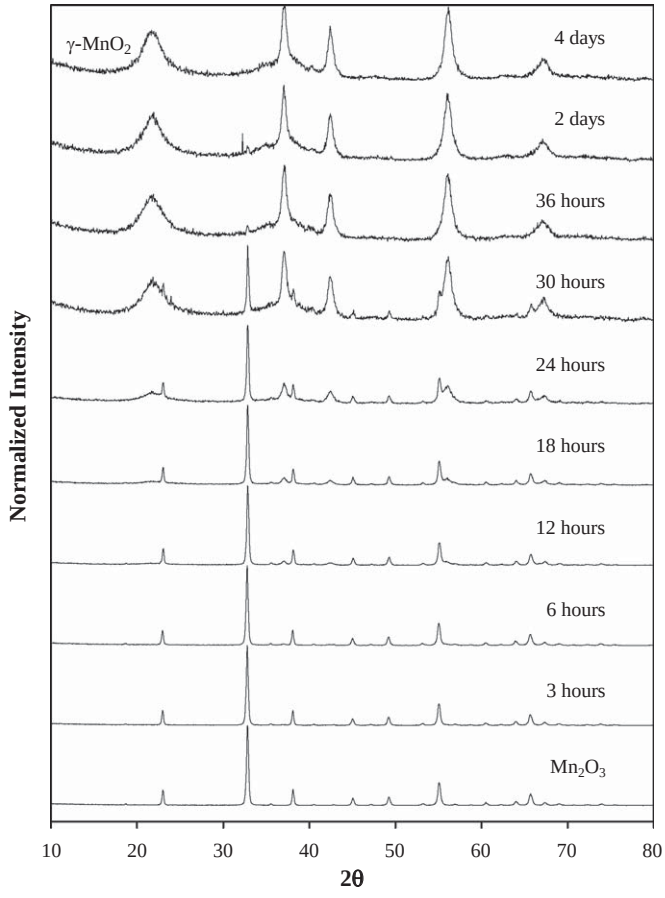

Fig. 3. Typical series of XRD pattern showing the conversion of Mn_2O_3 into MnO_2, in this case γ-MnO_2 (0.7 M H_2SO_4 at ambient temperature).

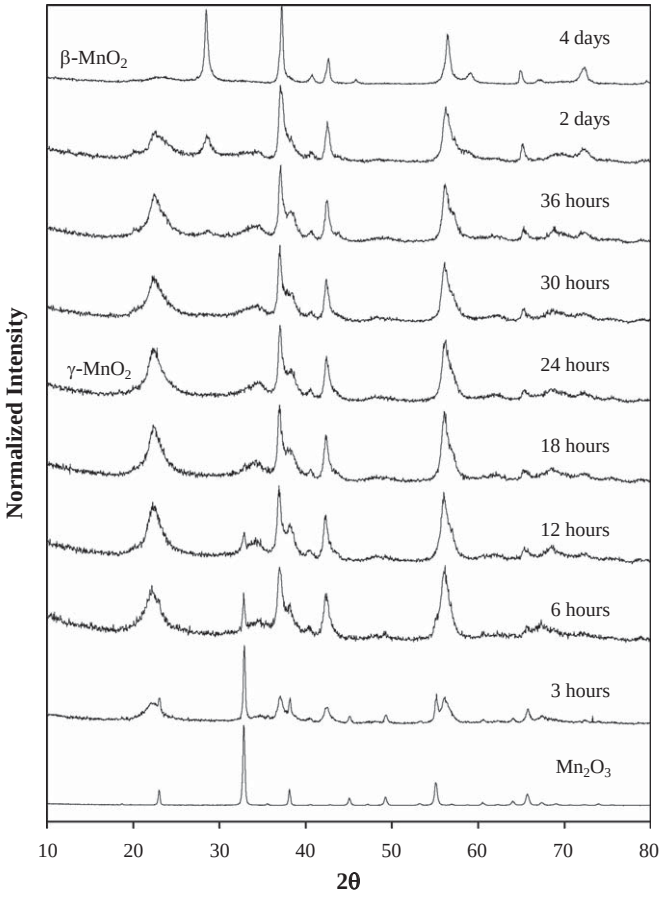

Fig. 4. Series of XRD patterns showing the conversion of Mn_2O_3 into γ-MnO_2 and then β-MnO_2 at elevated temperature (1.0 M H_2SO_4 at 80 °C).

represents only a metastable state. Ultimately, the γ-MnO_2 will convert to β-MnO_2, its just that the time frame of the experiments, particularly at lower temperatures, was not sufficiently long to observe this conversion.

To obtain kinetic data from the XRD patterns, particularly for the conversion of Mn_2O_3 to γ-MnO_2, we first fit a Lorentzian lineshape combined with a linear background to selected diffraction peaks in the range 19°–58°2θ; i.e.,

$$I = \frac{W^2}{4}\frac{I_{\max}}{(W/2)^2 + (2\theta - \mu)^2} \tag{9}$$

where I is the predicted normalized intensity, W is the peak width at half height (°2θ), $I_{\max}$ is the maximum normalized intensity and μ the peak position (°2θ). Linear least squares regression was used to minimize the difference between experimental and predicted curves. This analysis was carried out for peaks at 23.1°, 32.9° and 55.1°2θ representing Mn_2O_3, and those at 21.9° and 37.0°2θ for γ-MnO_2. Because the phases of manganese dioxide we are dealing with are quite disordered and hence have quite broad peaks (in particular the γ-MnO_2 phase) determining the proportion of each phase present in a mixture is best carried out using peak area rather than just the intensity. Therefore, for the selected peaks for each phase, the area under the curve was determined using numerical integration. All measured areas were then expressed relative to the corresponding peak area in the phase pure Mn_2O_3 and γ-MnO_2 samples. In this way the proportion of each phase present is expressed in terms of a mole fraction (X). A typical example of mole fraction as a function of time is shown in Fig. 5, this time for Mn_2O_3 digested in 2.0 M H_2SO_4 at 40 °C.

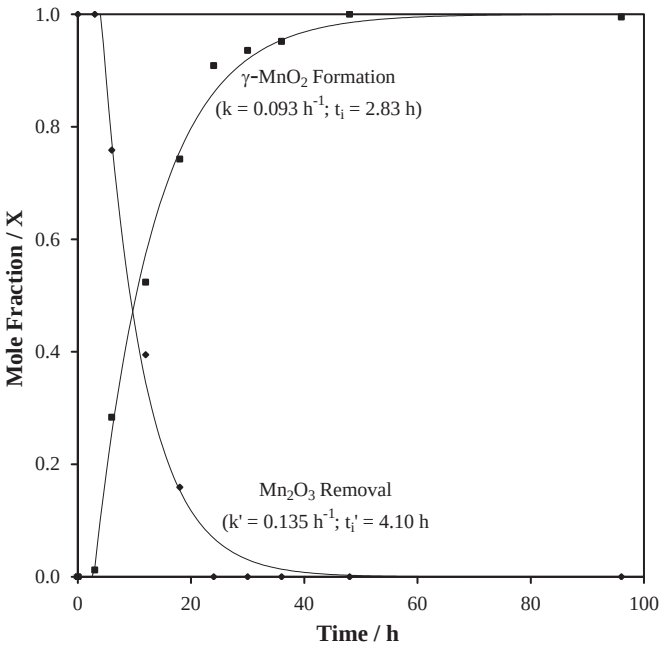

Fig. 5. Typical example of kinetic data extracted from the XRD data, in this instance for Mn_2O_3 digested in 2.0 M H_2SO_4 at 40 °C.

At this stage we have compositional information as a function of time for the digestion of Mn_2O_3 to γ-MnO_2. To quantify this conversion in terms of for instance a rate constant, a model is

needed to describe the digestion process. Numerous models have been developed to describe the structural conversion of solid state materials, including (i) the Avrami expression [17], in which the solid state transformation involves nucleation and growth stages, and (ii) the Jander expression [18], which is a three-dimensional diffusion controlled process. Of these, the use of Avrami expression was found to be most common [19], and so we have used it as the basis of our kinetic analysis. From the sample data shown in Fig. 5, it is apparent that there is a short induction period before the transformation begins. The origin of this induction period is probably saturation of the electrolyte with Mn(III) as a result of Mn_2O_3 dissolution before disproportionation occurs. Evidence to support this is in Fig. 5, where the disappearance of Mn_2O_3 occurs faster than γ-MnO_2 formation. To include this induction period, we have used a modified Avrami expression to model the formation of γ-MnO_2; i.e.,

$$X_{MnO_2} = 1 - \exp(-k(t - t_i))^n \quad (10)$$

where X_{MnO_2} is the mole fraction of manganese dioxide formed, k is the rate constant (h^{-1}), t is the time (h), t_i the induction time (h), and n is a constant whose value depends on the nature of the nucleation and growth process. Strictly speaking the Avrami expression employs the volume fraction rather than mole fraction [19]. In this work the measured densities of the two components were similar (4.70 g/cm^3 for Mn_2O_3 and 4.45 g/cm^3 for γ-MnO_2) meaning that the use of mole fraction is justified. While fitting Eq. (10) to experimental data (using linear least squares regression), we found that n almost always has a value close to unity ($0.95 < n < 1.05$), and so we have assumed $n = 1$ throughout. The implication of this result is that the transformation of Mn_2O_3 to γ-MnO_2 follows first-order kinetics. A similar expression to Eq. (10) can be deduced for Mn_2O_3 consumption; i.e.,

$$X_{Mn_2O_3} = \exp(-k'(t - t_i'))^{n'} \quad (11)$$

Fitted data based on Eqs. (10) and (11) have been included in Fig. 5. As can be seen in this figure, the greatest variability between experimental and predicted data occurs for Mn_2O_3 disappearance at low Mn_2O_3 mole fractions. The origin of this variability is most probably associated with extracting reliable peak fitting data from the XRD data when there is less than 10% of a phase present.

Eqs. (10) and (11) were applied to the kinetic data available, with the resultant rate constant data shown in Fig. 6(a) for Mn_2O_3 disappearance and Fig. 6(b) for γ-MnO_2 formation. As can be seen the rate constants increase dramatically as both acid concentration and temperature were increased. As mentioned in the Experimental, digestion experiments were also conducted at 100 °C; however, the rate of γ-MnO_2 formation was not able to be observed since it was overwhelmed by the formation of the thermodynamically stable product β-MnO_2, as suggested in Fig. 4. It is also apparent from the rate constants in Figs. 6(a) and (b) that Mn_2O_3 disappearance occurs faster than γ-MnO_2 formation, particularly at high acid concentrations and temperatures. The reason for this is due almost solely to the behaviour of the Mn(III) intermediate. In low acid concentration electrolytes very little soluble Mn(III) is formed because the equilibrium in Eq. (2) is a reactants orientated equilibrium (K_2 in Eq. (5)). As such, there are very few Mn(III) species liberated to solution and available for disproportionation to occur (Eq. (3)). This is despite the fact that this equilibrium is heavily products orientated. Hence the rate of this second step is limited by the formation of soluble Mn(III) species in the first step. As we move to more concentrated acid electrolytes, the concentration of soluble Mn(III) increases, as is the rate at which it forms, since in effect we have added more reactant to the system. At the same time, the rate of disproportionation is also expected to increase because again we have more

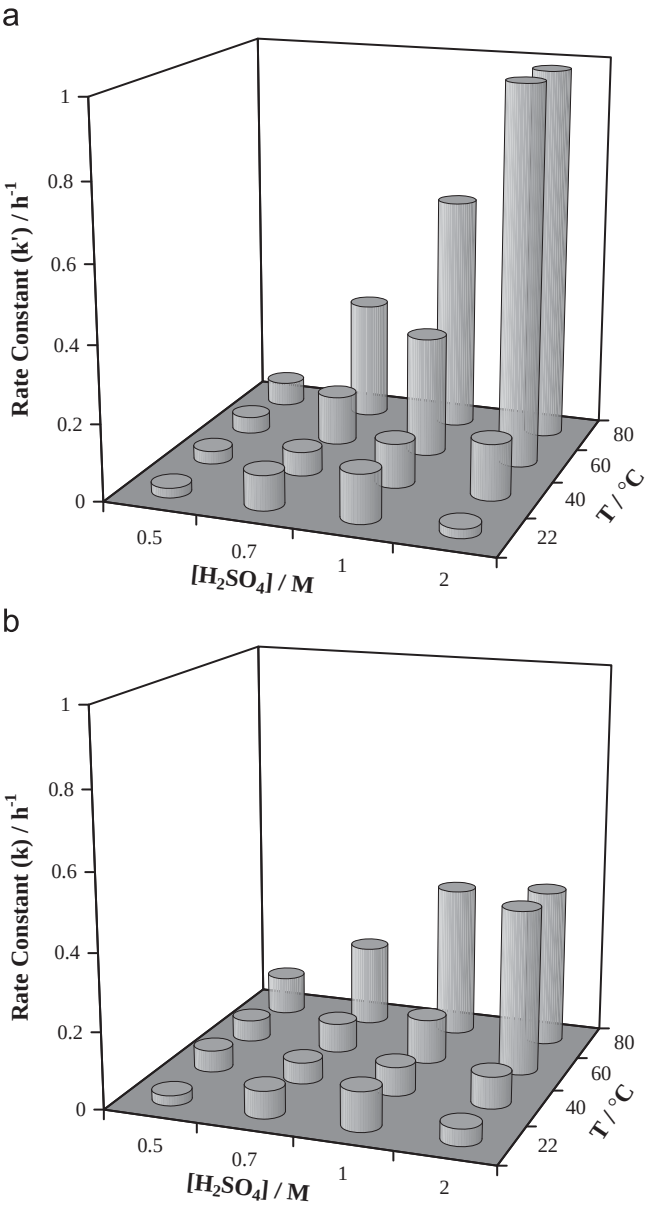

Fig. 6. Calculated rate constants for (a) the disappearance of Mn_2O_3 (k') and (b) γ-MnO_2 formation (k).

reactant available. While this explanation seems straightforward, the overall reaction rate is somewhat complicated by the inherent instability of the soluble Mn(III) species [13]. In low acid concentration electrolyte, soluble Mn(III) has limited stability, either hydrolysing and re-precipitating as Mn_2O_3, or disproportionating in contact with another Mn(III) species to form γ-MnO_2. An interesting question that arises here is whether the soluble Mn(III) species disproportionates with another soluble Mn(III) ion, or whether it disproportionates with solid Mn(III) on the substrate (Mn_2O_3) surface. Addressing this question is beyond the scope of the present communication. When the acid concentration increases so too does the stability of soluble Mn(III), to the point where a stable solution of Mn(III) species can be prepared. Under these conditions we are apparently losing the driving force for disproportionation to occur, potentially to the point where the disproportionation reaction becomes overall reaction rate limiting. However, in this work where we have limited the H_2SO_4 concentration to 2.0 M, Pourbaix [13] has indicated soluble Mn(III)

is still quite unstable, the rate constant data we have would suggest that this is not the case since γ-MnO_2 did indeed form. This apparent loss of driving force is most likely due to the absence of a suitable nucleation site, the formation of which takes more time, the more the acid concentration.

The induction time necessary for the disappearance of Mn_2O_3 and formation of γ-MnO_2 as functions of acid concentration and temperature are shown in Fig. 7(a) and (b), respectively. What is apparent from these data is that the use of low acid concentrations and temperatures results in a substantial induction time being necessary for reaction to occur, most likely for the reasons related to Mn(III) solubility and stability discussed previously. These data do show, however, that under the conditions considered, disproportionation of Mn(III) species with its required nucleation, does not lead to a noticeable induction period.

As we have already seen in Fig. 6, increasing the reaction temperature increases the rate of reaction. The basic equation

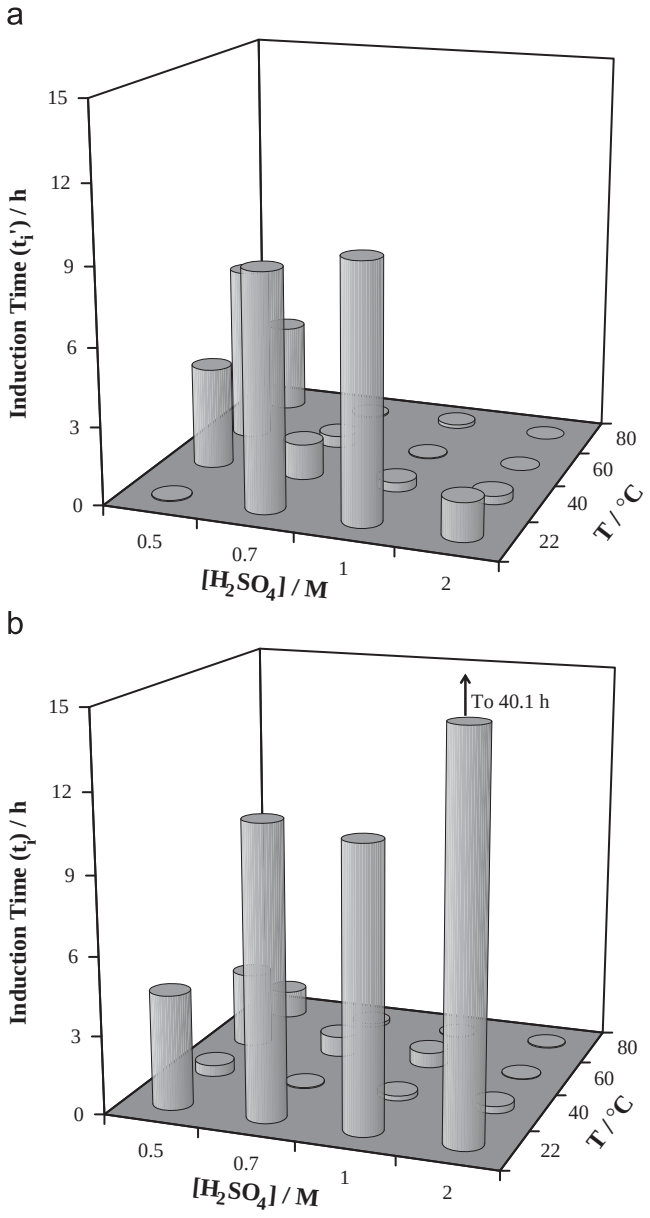

Fig. 7. Calculated induction times for (a) the disappearance of Mn_2O_3 (t_i') and (b) γ-MnO_2 formation (t_i).

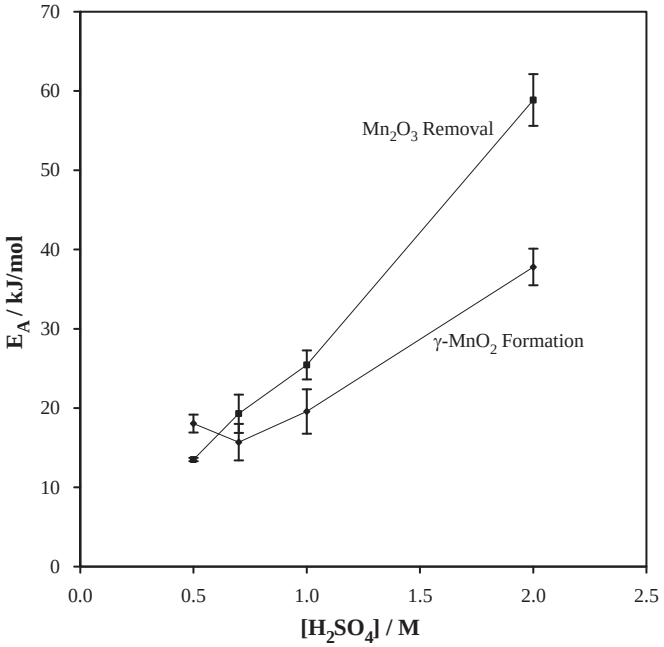

Fig. 8. Activation energies for Mn_2O_3 removal and γ-MnO_2 formation.

relating kinetic rate constants to the temperature of the reaction is the Arrhenius Eq. [19]; i.e.,

$$k = A\exp\left(\frac{-E_A}{RT}\right) \quad \text{or} \quad \ln(k) = \ln(A) - \frac{E_A}{RT} \tag{12}$$

where A is the pre-exponential factor (s^{-1}), E_A the activation energy for the process (J/mol), and R and T have their usual significance. After plotting ln(k/s) versus $1/(T/K)$ the activation energy for the overall reaction was determined, as shown in Fig. 8. This figure shows that the activation energy for Mn_2O_3 removal is almost always greater than the activation energy for the formation of γ-MnO_2, suggesting that it is the dissolution of Mn_2O_3 that is the rate determining step. The only exception is at the lowest acid concentration examined where the trend was reversed. In this case the effect of very low Mn(III) dissolution may have impacted on its subsequent disproportionation.

4. Summary and conclusions

The kinetics of Mn_2O_3 digestion in various H_2SO_4 solutions (0.5–2.0 M) and at various temperatures (ambient up to 80 °C) has been investigated using XRD. The digestion process has been broken down into two stages: namely; (i) dissolution of the Mn_2O_3 into soluble Mn(III) species in the electrolyte, which was monitored in the XRD data by the rate of Mn_2O_3 disappearance; and (ii) the disproportionation of soluble Mn(III) into manganese dioxide and soluble Mn(II), the kinetics of which were monitored in the XRD patterns by the rate of manganese dioxide formation. This range of H_2SO_4 concentrations and temperatures were chosen such that γ-MnO_2 was the phase of manganese dioxide produced. The kinetic data for both Mn_2O_3 disappearance and γ-MnO_2 formation were modelled using a first-order Avrami expression that had been modified to produce a rate constant (k), as well as an induction time (t_i) between when the experiment started and changes were observed to occur. Rate constants ranged from 0.02 to 0.98 h^{-1} for Mn_2O_3 disappearance and 0.03 to 0.42 h^{-1} for γ-MnO_2 formation. In all cases the rate constant for Mn_2O_3 disappearance was larger than that for γ-MnO_2 formation. Despite these values, it was also deduced that both steps in the

digestion limited the kinetics since the dissolution stage led to only very dilute soluble Mn(III) solutions, which in turn limited the rate of disproportionation. Overall the fastest kinetics were observed when more concentrated H_2SO_4 solutions (and hence greater Mn(III) solubility) and a higher temperature (expected) were used.

Acknowledgments

D.W. would like to acknowledge the receipt of an ADS scholarship as part of the AusAID scheme. He would also like to thank the Universitas Tadulako, Palu, for granting a leave of absence to continue his studies in Australia. Dr. Rodney Williams from Delta EMD Australia Pty Limited is also acknowledged for many technical discussions.

References

[1] Y.F. Yao, H.S. Wroblowa, J. Electroanal. Chem. 223 (1987) 107.
[2] P.M. de Wolff, Acta Crystallogr. 12 (1959) 341.
[3] [a] P. Ruetschi, J. Electrochem. Soc. 131 (1984) 2737;
[b] P. Ruetschi, J. Electrochem. Soc. 135 (1988) 2657;
[c] P. Ruetschi, R. Giovanoli, J. Electrochem. Soc. 135 (1988) 2663.
[4] R.P. Williams, Ph.D. Thesis, University of Newcastle, 1996.
[5] Y. Chabre, J. Pannetier, Prog. Solid State Chem. 23 (1995) 1.
[6] S. Turner, P.R. Buseck, Nature 304 (1983) 143.
[7] A.H. Heuer, A.Q. He, P.J. Hughes, F.H. Feddrix, ITE Lett. Batteries New Technol. Med. 1 (2000) 926.
[8] C.B. Ward, A.I. Walker, A.R. Taylor, Prog. Batteries Battery Mater 11 (1992) 40.
[9] [a] W. Feitknecht, W. Marti, Helv. Chim. Acta 28 (1945) 129;
[b] W. Feitknecht, W. Marti, Helv. Chim. Acta 28 (1945) 149;
[c] O. Glemser, G. Gattow, H. Meisiek, Z. Anorg. Allg. Chem. 309 (1961) 1;
[d] Y.F. Yao, H.S. Wroblowa, J. Electroanal. Chem. 223 (1987) 107.
[10] [a] W. Feitknecht, W. Marti, Helv. Chim. Acta 28 (1945) 149;
[b] O. Glemser, G. Gattow, H. Meisiek, Z. Anorg. Allg. Chem. 309 (1961) 1;
[c] R.M. McKenzie, Miner. Mag. 38 (1971) 493;
[d] J.B. Fernandes, B.D. Desai, V.N. Kamat Dalal, J. Power Sources 15 (1985) 209;
[e] E. Narita, T. Okabe, Bull. Chem. Soc. Jpn. 53 (1980) 525.
[11] M.H. Rossouw, D.C. Liles, M.M. Thackeray, Prog. Batteries Battery Mater 15 (1996) 8.
[12] D.K. Walanda, G.A. Lawrance, S.W. Donne, J. Power Sources 139 (2005) 325.
[13] M. Pourbaix, Atlas of Electrochemical Equilibria in Aqueous Solutions, Pergamon Press, London, 1966.
[14] D.R. Lide (ed.), Handbook of Chemistry and Physics, 73rd ed. 1992.
[15] J.Y. Welsh, Electrochem. Tech. 5 (1967) 504.
[16] C.J. Brinker, G.W. Scherer, Sol–Gel Science: The Physics and Chemistry of Sol–Gel Processing, Academic Press, San Diego, 1989.
[17] M. Avrami, J. Chem. Phys. 7 (1939) 1103.
[18] W. Jander, Z. Anorg. Allg. Chem. 163 (1927) 1.
[19] A.R. West, Solid State Chemistry and its Applications, Wiley, New York, 1984.